Compatible Finite Elements For Glacier Modeling

Douglas J. Brinkerhoff, *University of Montana, Missoula, MT, 59812, USA*

Abstract—We describe the first application of two mixed finite element methods to the solution of the equations of glacier evolution under different simplifying assumptions, along with a framework for the fully implicit solution of the coupled velocity-thickness equations. The first method uses Raviart-Thomas elements for velocity and piecewise constants for thickness and is a reframing of a classic staggered-grid finite difference method to the case of unstructured triangular meshes. The second method uses Mardal-Tai-Winther elements for velocity and exhibits several desirable properties: second order convergence of velocity and near-exact mass conservation, while resolving both membrane and shear stresses and under the challenging conditions of thin ice and steep topography.*

Glaciers and Ice Sheets respond to climate change through interdependent surface melt and ice dynamics. Such responses are critical towards understanding future sea level rise, ecological perturbations from modified biogeochemistry and water availability, and hazards over multiple time scales. On account of the feedback between elevation and snowfall, glaciers often flow through steep places; indeed, glaciers in mountainous regions are currently losing mass at an outsized rate relative to their volume [1]. Simultaneously, mass loss driven by ice dynamics is often most apparent at marine termini. Predicting glacier evolution requires models that can correctly resolve the physics associated with both mountain and marine environments, and models must remain stable and mass conservative in the presence of extreme topography while still resolving membrane stresses. In this work we explore the application of a class of mixed finite elements, referred to variously as mimetic or compatible finite elements, to the problem of glacier flow.

Mixed finite elements posit that velocity $\mathbf{u}(\mathbf{x}, z, t)$ and ice thickness $H(\mathbf{x}, t)$ be discretized separately, and that their discrete approximations live in different function spaces with differing degrees of regularity. Combinations of these spaces can be formulated such that differential operators map without approximation from one space to another, and such combinations of spaces are termed compatible. Geophysical models have long taken advantage of such schemes, which have been shown to be free of spurious pressure modes and to have desirable conservation properties [2]. Indeed, staggered-grid finite difference methods (e.g. the C-grid) can be interpreted as a specialization of compatible finite elements to quadrilaterals.

Ice-sheet modellers have similarly used compatible elements for the shallow ice approximation (SIA), which simplifies the Stokes' equations by assuming that membrane and vertical resistive stresses are negligible and that the pressure field is hydrostatic, which is appropriate in regions with slow flow and a shallow aspect ratio. However, models of intermediate complexity that do not neglect membrane stresses, such as the Blatter-Pattyn [4] (BPA; which assumes hydrostatic pressure, negligible vertical resistive stresses, and relatively small bed slopes) and shallow shelf (SSA; as the BPA, but also neglecting vertical shear stresses) approximations, are often more appropriate. Implementations of these approximations (when coupled to the evolution of ice thickness) to date have used either specialized grids or equal-order discretizations with stabilization. Both structured [3] and dual [5] grids, when used in conjunction with the finite volume method are conservative and stable, but can be geometrically restrictive or require additional computational bookkeeping. 'Standard' equal-order finite elements with artificial viscosity or a streamline upwind Petrov-Galerkin
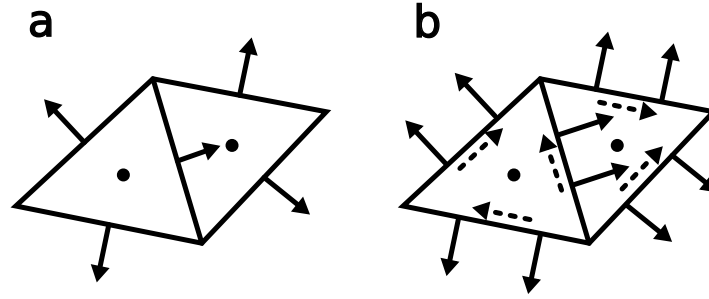
FIGURE 1. The degrees of freedom associated with (a) the mixed lowest-order Raviart-Thomas and zeroth order discontinuous Galerkin element and (b) the mixed Mardal-Tai-Winther and zeroth order discontinuous Galerkin element. Solid arrows represent moments of the velocity vector evaluated at the corresponding edge that lead to continuity between elements, while broken arrows represent moments that lead to a non-conforming approximation. The black dot represents element-wise constant geometric variables.

formulation are simple, efficient, and work well for regions of smooth surface and bed topography, but may yield oscillations in the presence of steep gradients and do not necessarily guarantee positivity of the thickness field, even in the absence of melt.

In an effort to extend the advantages of dual grid formulations to a single unstructured grid for solving the SIA, we first describe a compatible finite element pair, namely the lowest-order Raviart-Thomas element coupled with a zeroth order discontinuous Galerkin element. We use full nonlinear coupling for time integration, which allows large time steps. Because this discretization cannot resolve the membrane stresses present in the BPA and SSA, we modify our scheme to use the Mardal-Tai-Winther element which has the same favorable properties as the Raviart-Thomas space with additional smoothness. We evaluate these elements on some well-understood test cases and against a manufactured solution to confirm expected rates of convergence. Finally, to test the model under the motivating cases of both extreme topography and a marine terminus with real topography, we applied the model to the simulation of conditions reflective of the Pleistocene (including termination in a glacial lake) for a mountain basin in western Montana, where it exhibits desired properties of numerical stability and mass conservation.

EQUATIONS OF ICE FLOW

Ice sheet models solve for the ice thickness $H(\mathbf{x}, t)$ and velocity $\mathbf{u}(\mathbf{x}, z, t) = [u(\mathbf{x}, z, t), v(\mathbf{x}, z, t)]^T$. The evolution of the thickness is governed by the principle of mass

TABLE 1. Selected symbols used in this paper. Square brackets indicate a characteristic scale.

Symbol	Value	Description
$\mathbf{u}$		Ice velocity
$\dot{\epsilon}_1$		Strain rate tensor
η		Ice viscosity
H		Ice thickness
B		Ice base
S		Ice surface
δ	$[z]/[x]$	Aspect ratio
κ	$A^{\frac{-1}{n}}([u]/[z])^{(1-n)/n}$	Viscosity scale
γ	$[\beta][z](\rho_i g[z])^p/\kappa$	Friction scale
ω	$\rho_i g[z]^3/(\kappa[u][x])$	Driving stress scale
ζ	$[t][u]/[x]$	Flux scale
g	9.81 ms^{-2}	Gravitational acceleration
ρ_i	917 kg m^{-3}	Ice density
ρ_w	1000 kg m^{-3}	Water density
A	$10^{-16} \text{ Pa a}^{\frac{1}{n}}$	Ice softness
p		Sliding law pressure exponent
m		Sliding law velocity exponent
α		Impenetrability coefficient
β^2		Traction coefficient
$\dot{a}$		Mass balance
z_{topo}		Topography
z_{sl}		Sea level

conservation, which is expressed in non-dimensional form as a conservation law

$$\frac{\partial H}{\partial t} + \zeta \nabla_{\mathbf{x}} \cdot \bar{\mathbf{u}} H = \dot{a}, \quad H > 0 \qquad \text{on } \Omega \qquad (1)$$

$$\zeta (\bar{\mathbf{u}} H) \cdot \mathbf{n} = q_{in}, \qquad \text{on } \Gamma_{in} \qquad (2)$$

where an overbar indicates a vertical average, ζ a dimensionless flux scale (see Table 1), $\dot{a}$ the specific mass balance (i.e. the rate of ice-equivalent snowfall or melting), and $\nabla_{\mathbf{x}} \equiv [\frac{\partial}{\partial x_1}, \frac{\partial}{\partial x_2}]^T$.

Velocity is computed by solving the Blatter-Pattyn approximation to the Stokes equations, which balances viscous and gravitational driving stresses as

$$\nabla_{\mathbf{x},z} \cdot 2\eta \dot{\epsilon}_1 = \omega \nabla_{\mathbf{x}} S, \qquad \text{on } \Omega \qquad (3)$$

where ω is a stress scale, $\mathbf{S}(\mathbf{x}, t) = B(\mathbf{x}, t) + H(\mathbf{x}, t)$ the surface elevation, and $\nabla_{\mathbf{x},z} \equiv [\frac{\partial}{\partial x_1}, \frac{\partial}{\partial x_2}, \frac{\partial}{\partial z}]^T$. The elevation of the ice base is

$$B(\mathbf{x}, t) = \max \left(z_{sl} - \frac{\rho_i}{\rho_w} H(\mathbf{x}, t), z_{topo}(\mathbf{x}) \right), \qquad (4)$$

with z_{sl} the local sea level and $z_{topo}(\mathbf{x})$ the topography. As such, (3) applies to both grounded and floating ice. $\dot{\epsilon}_1$ is the strain rate tensor subject to the simplifications of the BPA:

$$\dot{\epsilon}_1 = \begin{bmatrix} \delta^2 \left(2\frac{\partial u}{\partial x_1} + \frac{\partial v}{\partial x_2} \right) & \frac{\delta^2}{2} \left(\frac{\partial u}{\partial x_2} + \frac{\partial v}{\partial x_1} \right) & \frac{1}{2}\frac{\partial u}{\partial z} \\ \frac{\delta^2}{2} \left(\frac{\partial u}{\partial x_2} + \frac{\partial v}{\partial x_1} \right) & \delta^2 \left(\frac{\partial u}{\partial x_1} + 2\frac{\partial v}{\partial x_2} \right) & \frac{1}{2}\frac{\partial v}{\partial z} \end{bmatrix} \qquad (5)$$

with δ the aspect ratio. The viscosity – which depends inversely on the effective rate of strain and thus describes a shear-thinning fluid – is given by Glen's flow law

$$\eta = (\dot{\epsilon}_{II}^2)^{\frac{1-n}{2n}}, \qquad (6)$$

with $\dot{\epsilon}_{II}$ the second invariant of the strain rate tensor.

At the surface and basal boundaries we impose stress-free and sliding conditions

$$2\eta \dot{\epsilon}_1 \mathbf{n} = \mathbf{0}, \qquad \text{on } \Gamma_S \qquad (7)$$

$$2\eta \dot{\epsilon}_1 \mathbf{n} = -\gamma \beta^2 N^p \|\mathbf{u}\|^{m-1} \mathbf{u}, \qquad \text{on } \Gamma_B, \qquad (8)$$

with β a friction coefficient, γ a dimensionless friction scale, N the effective pressure $\max(P_0 - P_w, 0)$, and m and p exponents on velocity or effective pressure that govern the non-linearity of the basal stress. At lateral domain boundaries, we typically impose a normal stress that corresponds to an impenetrable sidewall.

$$2\eta \dot{\epsilon}_1 \mathbf{n} = -\alpha(\mathbf{u} \cdot \mathbf{n})\mathbf{n}, \qquad \text{on } \Gamma_W, \qquad (9)$$

with α a (usually large) coefficient that governs the degree of normal 'friction' imposed at the boundary.

In practice, we utilize a terrain-following coordinate transformation $(\mathbf{x}, z) \rightarrow (\mathbf{x}', \varsigma)$ where $\varsigma = (S(\mathbf{x}) -$

$z) H(\mathbf{x})^{-1}$. Spatial derivatives in this coordinate system for an arbitrary function $f(\mathbf{x}, z)$ are

$$\frac{\partial f}{\partial x_i} = \frac{\partial f}{\partial x_i'} + \frac{\partial f}{\partial \varsigma}\frac{\partial \varsigma}{\partial x_i}, \qquad (10)$$

$$\frac{\partial f}{\partial z} = \frac{\partial f}{\partial \varsigma}\frac{\partial \varsigma}{\partial z}, \qquad (11)$$

with subsequent differential operators inheriting these definitions. We note that this coordinate system is undefined if the thickness goes to zero. As such, we conceptualize any margin as an 'ice cliff' of non-zero thickness, although this thickness may be quite small.

Weak Form

We discretize (1) and (3) by dividing the model domain Ω into single-layered prismatic cells $\Omega_T = \bar{\Omega}_T \times [0, 1]$ with lateral boundaries $\partial \Omega_T$, emphasizing that the unit thickness of the vertical dimension is a result of the coordinate transformation described previously. We obtain a weak form for a single cell by multiplying with test functions $\phi \in \mathcal{V}_\infty(\Omega_T)$ and $\psi \in \mathcal{V}_2(\bar{\Omega}_T)$ and integrating over Ω_T.

$$\int_{\bar{\Omega}_T} \psi \left(\frac{\partial H}{\partial t} - \dot{a} \right) \, dA - \int_{\bar{\Omega}_T} \zeta \left(\nabla_{\mathbf{x}} \psi \cdot \bar{\mathbf{u}} H \right) \, dA$$

$$+ \int_{\partial \bar{\Omega}_T} \zeta \left(\psi \mathbf{n}_{\mathbf{x}} \cdot \bar{\mathbf{u}} H \right) \, ds = 0, \quad \forall \psi \in \mathcal{V}_2(\bar{\Omega}_T), \qquad (12)$$

$$-\int_{\Omega_T} \nabla_{\mathbf{x},z} \phi : 2\eta H \dot{\epsilon}_1 \, dV - \int_{\Omega_T} \omega \left(\nabla_{\mathbf{x}} \cdot \phi H \right) S \, dV$$

$$-\int_{\bar{\Omega}_T} \left[\gamma \beta^2 N^p \|\mathbf{u}\|^{m-1} (\phi \cdot \mathbf{u}) \right]_{\varsigma=1} \, dA$$

$$+\int_{\partial \Omega_T} (\phi \otimes \mathbf{n}_{\mathbf{x}}) : 2\eta H \dot{\epsilon}_1 \, dA - \int_{\partial \Omega_T} \omega \left(\mathbf{n}_{\mathbf{x}} \cdot \phi H \right) S \, dA = 0,$$

$$\forall \phi \in \mathcal{V}_1(\Omega_T), \qquad (13)$$

with the appearance of the thickness in (13) resulting from the terrain-following coordinate, and where we have used boundary conditions (7) and (8) to eliminate integrals at the bottom and top of the prism.

COMPATIBLE ELEMENTS FOR THE SHALLOW ICE APPROXIMATION

We first consider the SIA, which can be derived from (13) by neglecting horizontal derivatives of the velocity or, equivalently, by setting $\delta \rightarrow 0$ in (5). To proceed we must specify function spaces $\mathcal{V}_1$ and $\mathcal{V}_2$.

Thickness space

We restrict our choice of $\mathcal{V}_2 \subset L^2(\bar{\Omega})$ to function spaces that are constant over an element (and thus discontinuous across element boundaries), namely the zeroth-order discontinuous Galerkin space (DG0). This space

is closely associated with the finite volume method and inherits its mass conservation properties as well as its tendency to preserve the monotonicity of solutions when paired with a carefully constructed transport scheme. It also inherits the necessity of specifying a numerical flux at mesh internal boundaries to couple adjacent cells. Summing (12) over all triangles

$$\int_{\bar{\Omega}} \psi \left(\frac{\partial H}{\partial t} - \dot{a} \right) \, \mathrm{d}A + \int_{\partial \bar{\Omega}} \zeta \, [\![\psi \mathbf{n_x}]\!] \cdot \widehat{\bar{\mathbf{u}} H} \, \mathrm{d}s,$$
$$+ \int_{\Gamma_{out}} \zeta \, (\psi \mathbf{n_x} \cdot \bar{\mathbf{u}} H) \, \mathrm{d}s = 0 \quad \forall \psi \in \mathcal{V}_2, \quad (14)$$

where $\partial\bar{\Omega}$ are the set of internal triangular mesh boundaries, $[\![\psi \mathbf{n_x}]\!] = \psi^+ \mathbf{n_x^+} + \psi^- \mathbf{n_x^-}$ is the jump of the test function and $\{H\}$ the average across a cell boundary, respectively, and $\widehat{\bar{\mathbf{u}} H}$ is a numerical flux, for which we use the Lax-Friedrichs flux

$$\widehat{\bar{\mathbf{u}} H} = \bar{\mathbf{u}} \{H\} + \frac{1}{2} |\bar{\mathbf{u}}| [\![H]\!]. \quad (15)$$

In order to maintain consistency between geometric variables, we discretize the bed topography z_B and the ice base B such that they live in $\mathcal{V}_2$ as well.

Velocity space

Next we select a function space for the velocity that is compatible with our chosen thickness space. Compatible spaces are constructed so that projection and differential operators commute, which means that the same result is obtained whether applying the operator before or after the approximation of the true function by its finite element approximation. This notion can be represented with the commutative diagram

$$\begin{array}{ccc} \mathbf{H}(\mathrm{div}) & \xrightarrow{\nabla \cdot} & L^2 \\ \downarrow{\scriptstyle \pi_1} & & \downarrow{\scriptstyle \pi_2} \\ \mathcal{V}_{1,\mathbf{x}} & \xrightarrow{\nabla \cdot} & \mathcal{V}_2, \end{array} \quad (16)$$

where π_1 projects vectors (such as $\bar{\mathbf{u}}$) and π_2 projects scalars (such as H). In this case, the relevant differential operator is the divergence, which appears in both (12) and (13), and because the system only requires that velocity (and its associated test function) have a well-defined divergence, we formally seek $\bar{\mathbf{u}} \in \mathcal{V}_{1,\mathbf{x}} \subset \mathbf{H}(\mathrm{div}, \bar{\Omega})$ where

$$\mathbf{H}(\mathrm{div}, \bar{\Omega}) = \left\{ \mathbf{v} \in \mathbf{L}^2 : \nabla \cdot \mathbf{v} \in \mathbf{L}^2. \right\} \quad (17)$$

Compatible elements are useful here because they ensure that when we take an inner product between the divergence of a test function in $\mathcal{V}_1$ and a function in $\mathcal{V}_2$ – as is the case in the second term of (13) – that non-physical high frequencies in the thickness field are not inadvertently cancelled for the purposes

of computing a velocity solution, which would allow such spurious thickness modes to remain in the solution. More formally, compatible elements naturally satisfy the $\mathrm{inf} - \mathrm{sup}$ condition [6]. Indeed, the so-called 'checkerboard' instability has long been observed when attempting to solve Darcy, Stokes, and shallow water equations, which are structurally similar; we have also encountered such modes in our own efforts to solve (13) and (12) using the 'standard' finite element space CG1 for velocity components in conjunction with a DG0 thickness space, which do not satisfy the $\mathrm{inf} - \mathrm{sup}$ condition.

Discrete function spaces that are subsets of $\mathbf{H}(\mathrm{div})$ have vector-valued functions with normal components that are continuous across cell edges, but are tangentially discontinuous. Several choices exist for $\mathbf{H}(\mathrm{div})$ elements that are compatible with the DG0 element. We use the lowest-order Raviart-Thomas element (RT1), which has one degree of freedom per edge representing the average velocity normal to the edge. When combined with a DG0 thickness, this generalizes the C-grid (which also has edge-normal velocity components) to unstructured triangular meshes.

While $\mathbf{H}(\mathrm{div})$ regularity is sufficient for $\bar{\mathbf{u}}(\mathbf{x})$, the shear-stress terms in ς require that $\mathbf{u}(\mathbf{x}, \varsigma)$ have a continuous first derivative in the vertical dimension (ignoring in this work the fact that the SIA can be solved directly). To this end, we define the tensor-product element

$$\mathcal{V}_1(\Omega) = \mathcal{V}_{1,\mathbf{x}} \otimes \mathcal{V}_{1,z}, \quad (18)$$

with $\mathcal{V}_{1,z} \subset H^1([0, 1])$, where

$$H^1([0, 1]) = \left\{ v \in L^2([0, 1]) : \frac{\partial v}{\partial \varsigma} \in L^2([0, 1]) \right\}. \quad (19)$$

We specify $\mathcal{V}_{1,z}$ by directly enumerating its basis functions. In particular, we require that it be spanned by zeroth- and fourth-order monomials. If we choose bases that are orthogonal with respect to the L_2 inner product, then the velocity vector can be expanded as

$$\mathbf{u}(\mathbf{x}, \varsigma) = \bar{\mathbf{u}}(\mathbf{x}) + \mathbf{u}_d(\mathbf{x}) \left[\frac{1}{n+1} \left((n+2)\varsigma^{n+1} - 1 \right) \right], \quad (20)$$

which has the capacity to represent the exact SIA solution for a suitable quadrature rule. This form is particularly convenient in that the depth-averaged velocity appears directly as a degree of freedom, while the basis function corresponding to deformation integrates to zero with respect to ς.

Again summing over all elements, the global weak

form is

$$-\int_{\Omega} \nabla_{\mathbf{x},z}\phi : 2\eta H \dot{\epsilon}_1 \, \mathrm{d}V - \int_{\Omega} \omega \left(\nabla_{\mathbf{x}} \cdot \phi H\right) S \, \mathrm{d}V$$
$$-\int_{\bar{\Omega}} \left[\gamma\beta^2 N^p \|\mathbf{u}\|^{m-1}(\phi \cdot \mathbf{u})\right]_{\varsigma=1} \, \mathrm{d}A$$
$$-\int_{\partial\Omega} \omega \, [\![\mathbf{n_x} \cdot \phi H]\!]\{S\} \, \mathrm{d}A = 0,$$
$$\forall \phi \in \mathcal{V}_1(\Omega) \tag{21}$$

where we retain the full strain rate tensor, but recall that all terms in $\dot{\epsilon}_1$ involving horizontal derivatives are zero under the SIA. Gradients in 21 should be understood in the element-wise sense, which may lead to jumps across element boundaries for some finite element spaces (including the ones that we use here). We neglect these unless explicitly written. We note that we apply integration by parts to the driving stress; because S is discontinuous we must include another numerical pseudo-flux, and we take the average on each side of the cell boundary. Unlike in many treatments of the analogous shallow water equations, we do not split the driving stress into terms involving thickness gradients from those involving basal gradients; the current method treats these terms identically so that the scheme is well-balanced in the sense that it preserves 'lake-at-rest' solutions.

Discretization in time and numerical solution
We discretize in time with a $\theta-$method, and as such must solve a nonlinear system of equations involving both H and $\mathbf{u}$ at each time step, for which we use Picard iteration. The fully discrete linearized system is

$$\int_{\bar{\Omega}} \psi \left(\frac{H_{k+1} - H_k}{\Delta t} - \dot{a}_\theta^*\right) \, \mathrm{d}A + \int_{\partial\bar{\Omega}} \zeta \, [\![\psi\mathbf{n_x}]\!] \cdot \widehat{\mathbf{u}H^*} \, \mathrm{d}s,$$
$$+ \int_{\Gamma_{out}} \zeta \, \left(\psi\mathbf{n_x} \cdot \bar{\mathbf{u}}_\theta H_\theta^*\right) \, \mathrm{d}s = 0, \quad \forall\psi \in \mathcal{V}_2, \tag{22}$$

$$-\int_{\Omega_T} \nabla_{\mathbf{x},z}\phi : 2\eta_\theta^* H_\theta^* \dot{\epsilon}_{1,\theta} \, \mathrm{d}V - \int_{\Omega_T} \omega \left(\nabla_{\mathbf{x}} \cdot \phi H_\theta\right) S_\theta^* \, \mathrm{d}V$$
$$-\int_{\bar{\Omega}_T} \left[\gamma\beta^2 N^{p*} \|\mathbf{u}_\theta^*\|^{m-1}(\phi \cdot \mathbf{u}_\theta)\right]_{\varsigma=1} \, \mathrm{d}A$$
$$-\int_{\partial\Omega} \omega \, [\![\mathbf{n_x} \cdot \phi H_\theta^*]\!]\{H_\theta\} \, \mathrm{d}A$$
$$-\int_{\partial\Omega} \omega \, [\![\mathbf{n_x} \cdot \phi H_\theta]\!]\{B_\theta^*\} \, \mathrm{d}A = 0, \forall\phi \in \mathcal{V}_1(\Omega) \tag{23}$$

with

$$\widehat{\mathbf{u}H^*} = \{\bar{\mathbf{u}}_\theta H_\theta^*\} + \frac{1}{2}|\bar{\mathbf{u}}_\theta^*| [\![H_\theta]\!],$$

where an asterisk denotes a quantity computed from the previous iteration. There are options with respect to which variable to hold fixed when $\mathbf{u}$, H, or S appear

non-linearly. Through experimentation, we found that solving for (versus holding fixed) diffusive terms lead to better stability; for example, in the transport equation we use the lagged value of thickness and the new value of velocity (which depends on the thickness gradient). In order to avoid negative thicknesses resulting from a negative specific mass balance, at each Picard iteration, we set any thickness $H < 10^{-12}$ to $H = 10^{-12}$. We note that this projection step necessarily induces a mass conservation error in the sense that the volumetric change of ice over a finite time interval is not necessarily equal to the integrated surface mass balance over the same interval, a property that holds for all discrete time-integration schemes [7].

We implemented the model using Firedrake [8]. For integrals arising in the assembly of the finite element matrix we allow Firedrake to automatically determine a suitable quadrature rule. We use a direct method to solve the resulting (non-symmetric) linear system, and make no particular effort at optimization, leaving an evaluation of computational efficiency for later work.

Verification with the Halfar solution
We first evaluate the RT1-DG0 element on two scenarios with exact solutions. The simpler of the two cases, the 'Halfar solution' [9], models a radially symmetric ice mass that evolves with neither mass balance nor sliding. We began with an initial dome height of 3 km and radius of 500 km and allowed the model to evolve from $t_0 = 292$ a to $T = 10t_0$ with $\Delta t = \frac{t_0}{10}$. Fig. 2a shows the L_2 norm of the error relative to the exact solution (due to the discontinuous nature of the DG0 space, it is difficult to produce a meaningful comparison to a continuous function; as such, we first project the solution into a CG1 finite element space before computing the norm). The resulting error is linearly proportional to cell size, which is consistent with theory for DG0 (although it is worth noting that even higher order schemes would exhibit similar convergence due to the inability of the Halfar solution to be represented accurately in a piecewise polynomial basis). Under the chosen parameters, errors in time are substantially smaller than those in space. Fig. 2b shows the spatially resolved differences between the exact and true solution along a diagonal transect. The emergent pattern indicates a transport scheme that is somewhat too diffusive, which is expected with a Lax-Friedrichs flux. The volume change between the beginning and end of the simulation is proportional to machine precision times the number of time steps, indicating practically perfect mass conservation. This is also true if we use a time step $\Delta t = 9t_0$, such that our
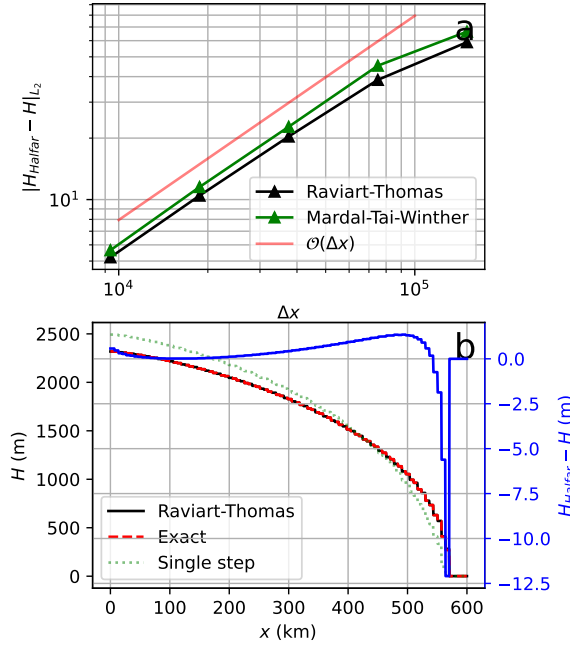
FIGURE 2. (a) The error in computed thickness at $t = 10t_0$ for the radially-symmetric, zero accumulation Halfar solution as a function of cell size for both the RT1-DG0 and MTW-DG0 elements. As expected on account of the DG0 discretization of thickness, both finite element pairs exhibits linear convergence in Δx. (b) The computed solution for the RT1-DG0 element as well as the spatially-resolved difference between predicted and modelled thickness.

time integration occurs in just a single time step. While such a solution is not particularly accurate, as shown in Fig. 2b, it remains stable and mass-conservative.

Verification of mass conservation in steep topography

To assess the performance of the method in steep topography, we also compare against the Jarosch-Schoof-Anslow solution [10], in which ice flows over a sheer cliff with surface mass balance defined such that the cliff is higher than the ice surface below it. Although such a circumstance violates the assumption of small bed slopes required in deriving the BPA and the SIA, it is nevertheless common in mountainous domains. This scenario is numerically challenging due to the tendency for models to produce spurious ice over discontinuities, leading to the expansion of the ice sheet past the location at which an along-flow integration of the surface mass balance function would place the margin. While the exact solution for this problem is one-dimensional, we simulated the problem
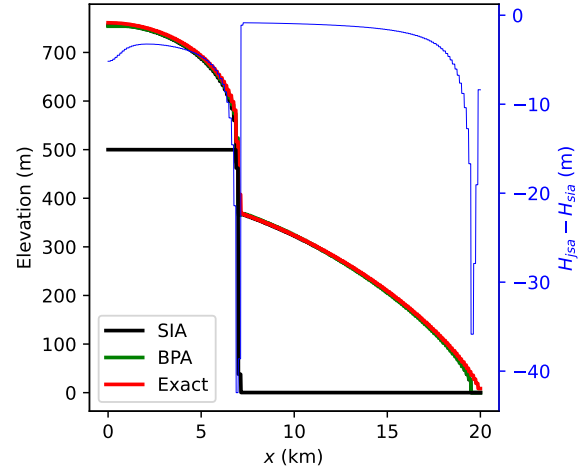

FIGURE 3. The exact and modelled steady-state surface elevation for flow over a bedrock step assuming the shallow ice approximation using both the RT1-DG0 and MTW-DG0 elements (which are indistinguishable), as well as the difference between the exact and modelled solutions. We also show the same test with membrane stresses included using the MTW-DG0 element, which deviates slightly from the SIA solution immediately in the vicinity of the step.

in two dimensions with a periodic boundary condition transverse to flow. Following 50 ka of time integration with $\Delta t = 20$ a and a nominal cell size of $\Delta x = 125$ m, we find a total modelled volume of 97.2% of the analytical steady state volume, which is a similar error to previous works [10]. We used $\theta = 1$, which allowed us to far exceed a quite-restrictive CFL criterion. The modelled solution is similar to the exact one (Fig. 3) but slightly thinner, again indicating an over-diffuse transport scheme.

COMPATIBLE ELEMENTS FOR THE BLATTER-PATTYN APPROXIMATION

We next turn to the development of a compatible finite element that resolves membrane stresses as well as vertical shearing. Once again, we restrict our search to a DG0 space for thickness, but no longer assume that membrane stresses are negligible. A tempting path would be to continue with RT1 elements as before. However, this approach will not be successful because membrane stresses require $\mathbf{u} \in \mathbf{H}^1$, where

$$\mathbf{H}^1 = \left\{ \mathbf{v} \in \mathbf{L}^2 : \frac{\partial \mathbf{v}}{\partial x_i} \in \mathbf{L}^2, \ i \in \{1, 2\} \right\}. \quad (24)$$

This is to say that both components of the velocity vector must have well-defined first derivatives, a

more stringent smoothness condition than $\mathbf{H}(\text{div})$ which only requires well-defined divergences. This resulting compatibility requirement corresponds to the modified commutative diagram

$$
\begin{array}{ccc}
\mathbf{H}^1 & \xrightarrow{\nabla \cdot} & L^2 \\
\downarrow{\scriptstyle \pi_1} & & \downarrow{\scriptstyle \pi_2} \\
\mathcal{V}_{1,\mathbf{x}} & \xrightarrow{\nabla \cdot} & \mathcal{V}_2
\end{array} \tag{25}
$$

which requires unusual finite element spaces. One element that was constructed to satisfy these requirements is the Mardal-Tai-Winther (MTW) element [11]. This element spans a vector-valued third degree polynomial space, with additional constraints of order one polynomials along element boundaries and a constant divergence, which requires two degrees of freedom per edge representing normal moments plus one degree of freedom per edge representing the first tangential moment (Fig. 1). With respect to the latter, the element is non-conforming in the sense that tangential velocity components are only continuous across element boundaries in the average rather than point-wise sense. The MTW element was originally developed for incompressible Darcy-Stokes flow, which has substantial similarities to the BPA in that solutions live in $\mathbf{H}^1$ in the Stokes flow limit and $\mathbf{H}(\text{div})$ in the Darcy limit. Furthermore, it was designed to be compatible with DG0 pressure fields.

The solution procedure for the MTW-DG0 scheme is identical to that described above for the RT1 element, with two exceptions. First, boundary conditions are imposed by adding a weak form of (9) to (21). Second, we require explicit gradients of the ice thickness and base to account for the extra derivative terms arising from the ς-coordinate transformation. We accomplish this efficiently through a projection, solving at each Picard iteration the linear equation for $\widehat{\nabla}_{\mathbf{x}} B \in \mathcal{V}_{1,\mathbf{x}}$

$$
\int_{\bar{\Omega}} \phi \cdot (\widehat{\nabla}_{\mathbf{x}} B) = - \int_{\bar{\Omega}} (\nabla_{\mathbf{x}} \cdot \phi) \, B \, dA + \int_{\partial \bar{\Omega}} [\![\mathbf{n}_{\mathbf{x}} \cdot \phi]\!] \{B\} \, ds
$$
$$
\forall \phi \in \mathcal{V}_{1,\mathbf{x}}, \tag{26}
$$

(and similarly for the gradient of $\mathbf{H}$) which is positive definite and converges in just a few iterations of conjugate gradient.

Validity of the Mardal-Tai-Winther element in the SIA limit

Because $\mathbf{H}^1 \subset \mathbf{H}(\text{div})$, and because both elements are compatible with DG0, the MTW element should perform similarly to the RT1 element under the SIA assumption. To show that this is the case, we performed both numerical experiments described in the
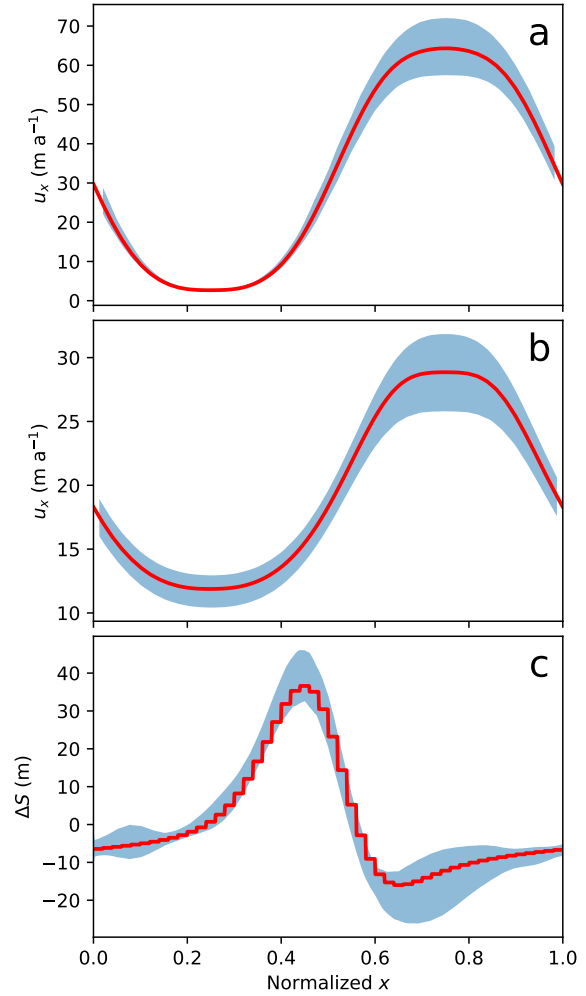

FIGURE 4. The velocity at $y = L/4$ for $L = 40$km for the ISMIP-HOM intercomparisons experiments A (a) and C (b), and (c) the steady state surface elevation anomaly for the 'slip' variant of experiment F (note that we have retained the discontinuous character of the solution, accounting for the stair step pattern. Shaded region indicates two standard deviations in the ensemble of higher-order solutions submitted for the original ISMIP-HOM.

previous section with the RT1 element replaced with the MTW element. In both cases (Fig. 2 and Fig. 3) we find the solutions to be nearly identical. Of course we do not advocate for the MTW element to be used for SIA models, since it has triple the degrees of freedom. However, such tests indicate that it inherits the simpler element's stability and accuracy properties.

Intercomparison with ISMIP-HOM

The principle advantage of the MTW element relative to RT1 is its capacity to correctly resolve membrane stresses. We assessed this by applying the scheme to the ISMIP-HOM intercomparison experiments [12], which test models on simplified geometries at various length scales. Figs. 4a,b show the respective velocity solutions for ISMIP-HOM A, which describes non-slip flow over a bed that varies sinusoidally in both dimensions; and ISMIP-HOM C, which describes flow over a flat bed with sinusoidal basal traction, both evaluated at the $L = 40$ km length scale (results are similar for other length scales omitted for brevity). In both cases, the solutions produced by the MTW element agree well with the distribution of the benchmark ensemble. Indeed, for ISMIP-HOM C we find that our solutions agree closely with full Stokes solutions at all length scales, which is consistent with an asymptotic analysis of the BPA. We also performed ISMIP-HOM F, which tests the model's prognostic solution capacity through periodic flow over an isolated Gaussian bump. Fig. 4c shows that the steady state surface elevation agrees well with the benchmark ensemble.

Verification with the Method of Manufactured Solutions

As a final verification step, we assessed the convergence of the MTW-DG0 element pair under both spatial and temporal refinement using the method of manufactured solutions. We note that we performed these tests under the assumptions of the shallow shelf approximation, in which we neglect the second, vertically varying basis function in $\mathcal{V}_{2,z}$. The reason for this is that because the vertical basis is not complete, there is no notion of refinement under which convergence to an exact solution could be achieved (despite it being a good ansatz for vertical variation in ice velocity, as indicated by the results of the previous section).

To construct a (non-dimensional) manufactured solution, we assumed a bed elevation given by

$$B(\mathbf{x}) = \cos(2\pi x_1) \cos(2\pi x_2) \qquad (27)$$

and a constant basal traction of $\beta^2 = 10^{-1}$, with $p = 0$. We assumed an analytical ice surface solution of

$$S_{mms}(\mathbf{x}, t) = \exp(-t/T) \cos(2\pi x_1) \cos(2\pi x_2) + C, \qquad (28)$$

with $T = 25$ and $C = 2$. The manufactured thickness solution is then $H_{mms} = S_{mms} - B$. We specified velocity solutions so that the resulting artificial forcing functions
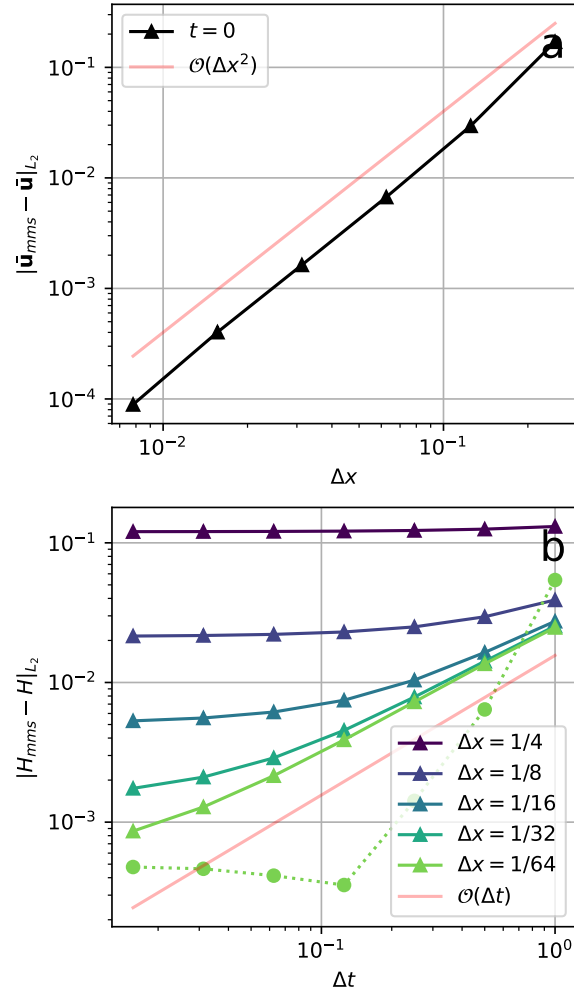

FIGURE 5. (a) The error in computed velocity at $t = 0$ against a manufactured solution as a function of cell size, which exhibits second order convergence. (b) The error in computed thickness at $t = T$ against a manufactured solution as a function of time step for multiple cell sizes using the shelfy-stream approximation. Note the expected linear convergence except when spatial discretization error creates a plateau. The dotted line shows second order convergence in time step for the finest spatial resolution with $\theta = \frac{1}{2}$, i.e. Crank-Nicholson.
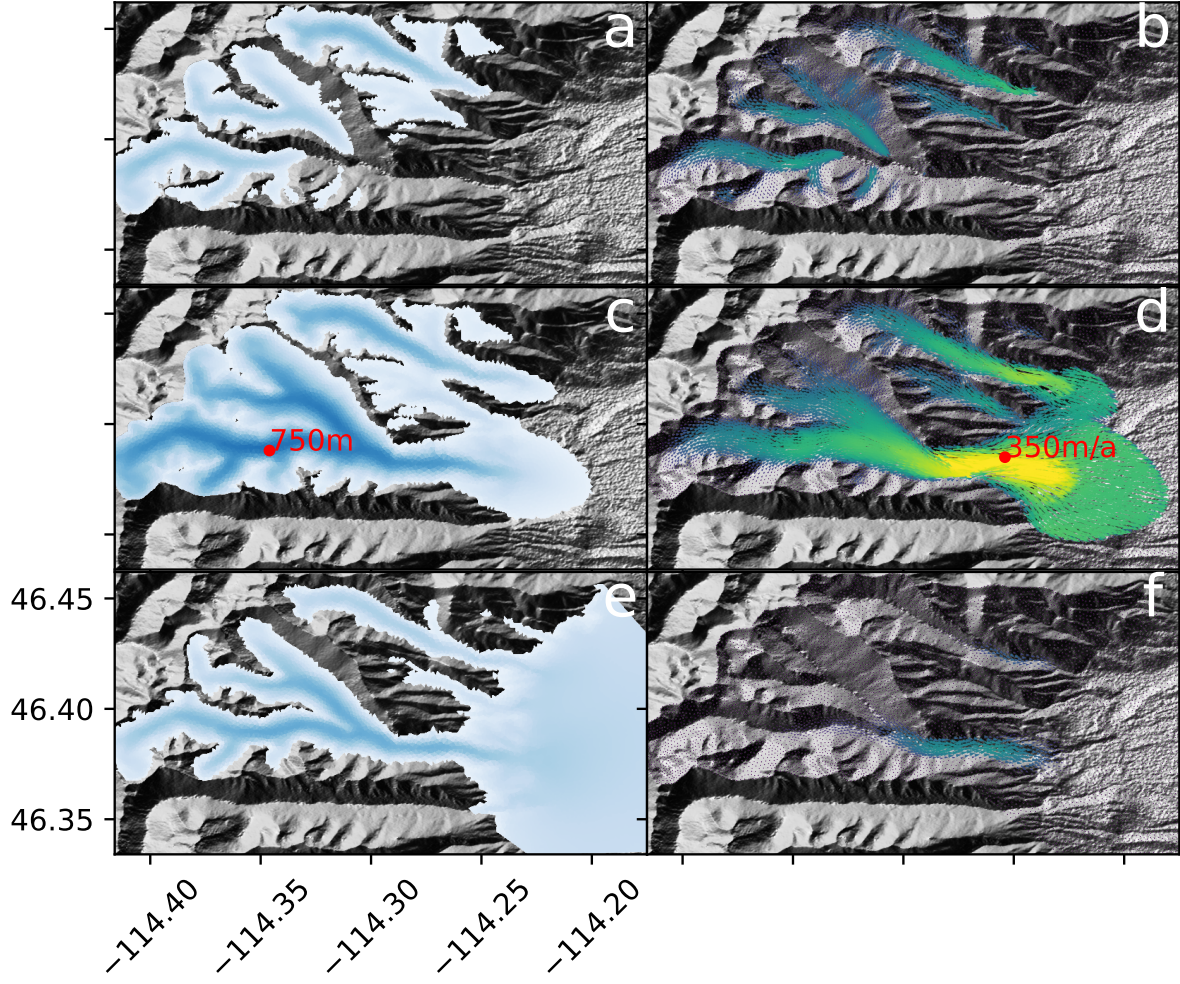
FIGURE 6. The evolution of the thickness and and velocity fields for our realistic steep-topography experiment during the glacier's growth (t = 200a; a and b), at a steady glacial maximum (t = 1000a; c and d) and following an additional 1000 years of evolution in the absence of any accumulation or ablation (e and f).

are relatively small, with

$$\mathbf{u}_{mms}(\mathbf{x}, t) = k_{mms} \exp(-t/T) \begin{bmatrix} \sin(2\pi x_1) \cos(2\pi x_2) \\ \cos(2\pi x_1) \sin(2\pi x_2) \end{bmatrix},$$
(29)

and $k_{mms} = 10^{-1}$. Such a solution is consistent with periodic boundary conditions, which we applied for both thickness and velocity. Because the computation of the manufactured source term by application of the strong form of the SSA and transport equations is error prone, we used Firedrake's symbolic manipulation capabilities to derive the residual automatically.

Fig. 5a shows the error under grid refinement of the velocity solution at $t = 0$. We find that the element combination achieves expected second-order conver-

gence. Fig. 5b shows the CG1-projected thickness error at $t = T$ under varying choices of grid and time step refinement for $\theta = 1$. We find that so long as the error is not overwhelmed by the spatial discretization, then our method achieves expected linear convergence. Using $\theta = \frac{1}{2}$, we achieve convergence proportional to Δt^2, but observe less robust convergence of the nonlinear solver when applied to domains with realistic topography.

APPLICATION TO REALISTIC TOPOGRAPHY

As a final test of the MTW-DG0 element and our solver, we performed a two-stage simulation with real
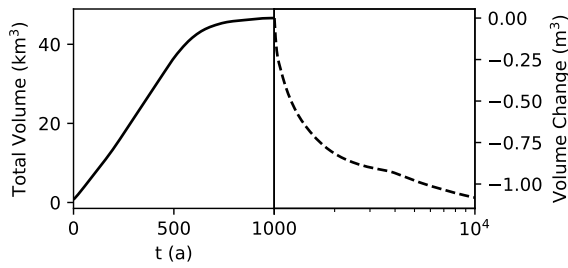
FIGURE 7. The ice volume through time for our realistic steep-topography experiment. During the first 1000 years of the simulation, we build a glacier using the mass balance function described in the text. At $t = 1000$ a the surface mass balance is set to uniformly zero, which in tandem with a no-flux boundary condition should yield exact maintenance of volume through time (note the change in scale for both axes). At $t = 10\,000$ a, we see a volume change of roughly -1 m^3, which is consistent with accumulating numerical roundoff error.

topography from Bear and Sweathouse Creeks in the Bitterroot Mountains of western Montana, USA. While both drainages are currently unglacierized, Pleistocene glaciation incised deep canyons with extremely steep walls and hanging valleys into the metamorphosed granite of the Idaho Batholith, creating suitably challenging conditions under which to test stability and mass conservation. Glacial Lake Missoula also filled the broad canyon mouths, which we include to test the model's capacity for simulating floating ice and a mobile grounding line (although we neglect calving).

We generated a mesh by automatically delineating watershed boundaries in the high elevation mountains and manually delineating arbitrary domain edges in the lower valley (See Fig. 6). The nominal spatial resolution is 150 m, for a total of 16 000 cells. We used a maximum time step of $\Delta t = 10$ a, but this was occasionally reduced automatically (and then increased again) when the Picard iteration fails to converge within 10 iterations. For reference, each time step took roughly 4 seconds running on four Intel i7-11800H 2.30GHz cores. The maximum and minimum elevation are approximately 2300 m and 1100 m respectively, with a lake level of 1500 m. We set $\beta^2 = 100$ m^{-1}a, $p = 1$, set the water pressure to the greater of three quarters of overburden or the depth below lake level. Importantly, we imposed zero-flux boundary conditions along all external edges, and thus no mass entered or left the system except through surface mass balance.

In the first stage of our test, we built glaciers by im-

posing the elevation-dependent specific mass balance

$$\dot{a} = 5 \text{ a}^{-1}(S - 2100 \text{ m}), \tag{30}$$

which yielded accumulation on only the highest peaks, as shown in Fig. 6a,b. We evolved the system under this mass balance function for 1000 a, reaching an approximate steady state (Fig. 6c,d. The resulting maximum thickness is 750 m with maximum velocity of 350 ma^{-1}. We note the development of substantial floating ice.

In the second stage, we set the specific mass balance to $\dot{a} = 0$ and allowed the system to evolve for an additional 9000 a, which is shown in Fig. 6e,f. Because of the no-flux boundary condition, ice in the (former) accumulation area flowed into the valley and stagnates in a large, flat pool. Remaining ice in steep areas became very thin (often millimeters or less). While not a scenario that mirrors anything of particular physical relevance, this scenario allows us to evaluate the model's capacity to conserve mass under such conditions. Fig. 7 shows a time series of total mass for both stages. In this second stage, the mass changed by approximately -1 m^3 at the end of the simulation, which is consistent with accumulated round-off error. As such, the element described here has satisfactory mass-conservation properties and can easily simulate glaciation and deglaciation without numerical issues.

CONCLUSION

In this work, we have described the first application of two mixed finite element methods to the equations of glacier motion, along with a fully-coupled implicit time integration method. The resulting models are stable, exhibit the expected errors, are locally mass-conservative and positivity preserving, and are free of spurious thickness modes. They are also relatively simple in the sense that they operate only on the cells and edges of a standard triangular grid. As such, this model is a practical choice for modeling many glaciological scenarios. Both elements are well-suited for simulations with steep topography and the MTW-DG0 element can also accurately characterize membrane stresses.

The model presented here has a few important limitations that also suggest some future goals. First, because we use a DG0 element for thickness, the spatial accuracy of the method is linear in mesh resolution. This could be improved with higher-order DG elements for thickness, but would require the development of new compatible elements; implementation of such new elements is made easier with modern finite element libraries such as Firedrake. While we did not explore

the accuracy of grounding line and calving front resolution, higher order elements could be particularly useful for their resolution through *p*-refinement. Finally, much work is still needed to develop linear and non-linear solvers optimized for these finite element pairs.

REFERENCES

1. D. R. Rounce, R. Hock, F. Maussion, R. Hugonnet, W. Kochtitzky, M. Huss, E. Berthier, D. Brinkerhoff, L. Compagno, L. Copland, D. Farinotti, B. Menounos, and R. W. McNabb, "Global glacier change in the 21st century: Every increase in temperature matters," *Science*, vol. 379, no. 6627, pp. 78-83, 2023.

2. T. H. Gibson, A. T. McRae, C. J. Cotter, L. Mitchell, and D. A. Ham, "Compatible Finite Element Methods for Geophysical Flows: Automation and Implementation Using Firedrake," *Springer Nature*, 2019

3. S. Cornford, D. Martin, D. Graves, D. Ranken, A. Le Brocq, R. Gladstone, A. Payne, E. Ng, and W. Lipscomb, "Adaptive mesh, finite volume modeling of marine ice sheets," *Journal of Computational Physics*, vol. 232, no. 1, pp. 529–549, 2013.

4. F. Pattyn, "A new three-dimensional higher-order thermomechanical ice sheet model: Basic sensitivity, ice stream development, and ice flow across subglacial lakes," *Journal of Geophysical Research: Solid Earth*, 108(B8), 2003.

5. M. Hoffman, M. Perego, S. Price, W. Lipscomb, T. Zhang, D. Jacobsen, I. Tezaur, A. Salinger, R. Tuminaro, and L. Bertagna, "MPAS-Albany Land Ice (MALI): a variable-resolution ice sheet model for Earth system modeling using Voronoi grids," *Geosci. Model Dev.*, vol. 11, pp. 3747-–3780, 2018, doi:10.5194/gmd-11-3747-2018.

6. D. Boffi, B. Franco, and M. Fortin. "Mixed finite element methods and applications," vol. 44. Heidelberg, Germany: Springer, 2013.

7. E. Bueler, "Conservation laws for free-boundary fluid layers," *SIAM Journal on Applied Mathematics*, 81(5), 2007-2032, 2021.

8. F. Rathgeber, D. Ham, L. Mitchell, M. Lange, F. Luporini, A. Mcrae, G.-T. Bercea, G. Markall, and P. Kelly, "Firedrake: automating the finite element method by composing abstractions," *ACM Trans. Math. Softw.*, vol. 43, no. 3, 2016, doi:10.1145/2998441.

9. E. Bueler, C. Lingle, J. Kallen-Brown, D. Covey, and L. Bowman, "Exact solutions and verification of numerical models for isothermal ice sheets," *Journal of Glaciology*, vol. 51, no. 173, pp. 291-306, 2005.

10. A. Jarosch, C. Schoof, and F. Anslow, "Restoring mass conservation to shallow ice flow models over complex terrain", *The Cryosphere*, vol. 7, pp. 229-–240, 2013, doi:10.5194/tc-7-229-2013.

11. K. Mardal, X. Tai, and R. Winther, "A robust finite element method for Darcy–Stokes flow," *SIAM Journal on Numerical Analysis*, vol. 40, no. 5, pp. 1605–1631, 2002.

12. F. Pattyn, L. Perichon, A. Aschwanden, B. Breuer, B. De Smedt, O. Gagliardini, G. H. Gudmundsson et al. "Benchmark experiments for higher-order and full-Stokes ice sheet models (ISMIP–HOM)," *The Cryosphere*, vol. 2, no. 2, pp. 95–108, 2008.

Douglas J. Brinkerhoff is an assistant professor at the University of Montana, Missoula, MT, USA. His research interests include finite element analysis, Bayesian inference, and ice sheet modeling. He received the Ph.D. degree in geophysics from the University of Alaska Fairbanks. He is a scientific editor for the Journal of Glaciology. Contact him at doug.brinkerhoff@mso.umt.edu.